Journal of Science and Technology in Civil Engineering, NUCE 2021. 15 (2): 90–100

GENERAL NON-UNIFORM QUADRILATERAL CROSS-SECTIONS FOR THIN-WALLED FG SANDWICH BEAMS

Tan-Tien Nguyen[a], Quoc-Hung Nguyen[a,*], Thang D. Le[a], Hiep D. Le[a]

[a]*Faculty of Engineering, Vietnamese-German University,*
Le Lai street, Thu Dau Mot city, Binh Duong province, Vietnam

Article history:
Received 23/02/2021, Revised 04/03/2021, Accepted 29/03/2021

Abstract

The paper aims at introducing an analysis of thin-walled functionally graded sandwich beams for general non-uniform quadrilateral cross-sections. Generally, the materials are assumed to be graded through the thickness following a predefined shape while Poisson's ratio kept as a constant due to its less domination. The cross-section linearly varies from one end to another end of the beam. In order to relax the difficulties in modeling as well as capturing the behaviors of thin-walled functionally graded beams, a higher-order approach has been applied including warping, coupling distortions as well as Poisson's distortion. A multi-separated beam on each edge of the cross-section which is an application of the so-called beam-frame-modal method is adopted. Subsequently, the effects of these major importance along with anisotropy of materials are then fully considered. As a consequence, the analysis is able to extensively applied to closed-section beam-shells with different curvatures. In order to illustrate the accuracy and computational efficiency of the method, various examples have been conducted in which the results obtained from finite element package as ABAQUS are employed.

Keywords: quadrilateral cross-section; thin-walled FG beam; higher-order coupling; beam frame modal.

https://doi.org/10.31814/stce.nuce2021-15(2)-08

1. Introduction

Recent years have seen many applications of the novel Functionally Graded Materials (FGMs) [1] and thin-walled structures [2]. Due to its high strength-to-weight ratio and effectiveness-thermal resistance, FGMs continues to be one of ideal candidates that may be superseded conventional multi-layer materials in the near future that widely applied in various areas, e.g. aerospace technology, automobile, submarine structures, etc. The advantages of FGMs can be explained by the fact that abrupt transitions from one to another material surface are completely eliminated. As a result, cracking or inter-lamina stresses has been tackled in a better performance.

Given the very first analysis of the thin-walled structures, a considerable attention had been gained by Vlasov [3] and other authors [4–6]. The analysis was normally performed by considering a linear warping, however some effects, e.g. distortion, higher-order warping, were somewhat underestimated. Consequently, analytical solutions were provided [7, 8]. Moreover, to further facilitate in solving governed equations, several finite element methods had been established and then found to be conveniently effective whereas shear strain at mid-surface was usually neglected [9].

*Corresponding author. *E-mail address:* hung.nq@vgu.edu.vn (Nguyen, Q.-H.)

With the potential application of thin-walled structures, the theory has remarkably been improved over the years. Kollár et al. [10], for example, obtained a closed form solution for flexural-torsional buckling problems of thin-walled open section columns in which both restrained warping and shear deformation effects were taken into account. Recently, Nagashima et al. [11] successfully developed X-FEM model for buckling analysis of thin-walled composite structures with delaminations that significantly reduced computational cost since additional works such as meshing or DOFs increasing were not strictly required.

More recently, Kim et al. [12] performed a study of static and vibration problems concerned with single and multi-cell cross-sections. As reported by the authors, a general varying cross-section as well as higher-order approaches had utilized. As a consequence, the effectiveness and accuracy were proven quite favorable.

In parallel to the development of computer science and automation technology, e.g. 3D printer technique that enables the advanced FGMs fabrication to be increasingly accessible, many efforts have been made. Among studies found in the literature, a very first investigation was introduced by Aboudi et al. [13]. As reported in the paper, a higher-order theory of functionally graded materials was fully expanded for a variety of structures together with uniform and gradient thermomechanical loadings. Wali et al. [14] analyzed FGM shell structures by means of a double directors shell element whereas the shear correction factor was totally removed. Regards to thin-walled beams, Librescu et al. [15] presented a comprehensive study on static and eigenvalue problems of spinning beams. From the paper, the material variation was assumed to be graded through the thickness direction following a simple law distribution of the constituent phases such as metal or ceramic.

From all above-mentioned studies and highlights, there also remands a need in developing a conforming approach for the applicability of thin-walled quadrilateral cross-section beams with functionally graded materials. The analysis, therefore, is able to achieve accurate results of the behavior of the beam as well as offering a profitably potential application in practical engineering design.

Primarily, the paper emphases on thin-walled beam modeling with functionally graded materials that provides one hand a highly accurate solution based on a finite element method with higher-order consideration of warping and distortions, reflects on the other hand a computational efficiency for deeper investigating towards FG materials, interaction of geometric features as well. The model is validated via several tests from available FEM tools as ABAQUS. In addition, some aspect ratios, e.g. material variations, skin-core-skin thickness have also parametrically investigated.

2. Theory of thin-walled beam

2.1. Kinematics

Along axial direction, the displacements of a point for general positions on a cross-section are obtained by using a combination of one-dimensional translation and rotation as well as several higher-order modes. Based on stress-strain relations, material transformation, governing equations are then established by means of the principle of the minimum potential energy.

In general, the contour displacements on the general quadrilateral cross-section as described in Fig. 1 can be calculated as:

$$\bar{\mathbf{u}} = \mathbf{\Psi} \cdot \mathbf{U} \tag{1}$$

where

$$\bar{\mathbf{u}} = \begin{Bmatrix} \bar{u}_n \\ \bar{u}_s \\ \bar{u}_z \end{Bmatrix} \tag{2}$$

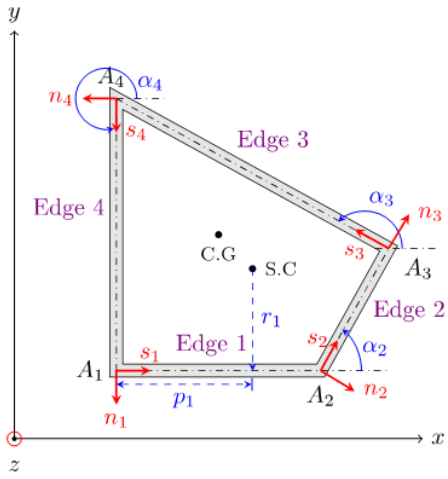

Figure 1. Geometries and coordinates of a thin-walled quadrilateral cross-section

where s, n-axes are in-plane coordinates that are tangential and normal to the mid-surface of a cross-section, respectively, and z-coordinate is set to parallel to the axial direction of the beam. In Fig. 1, α_i refers to the angle corresponding to edge i^{th} and the x-axis whereas r_i, p_i are the distances calculated from the shear center to the center line of edge and the vertex i^{th}, respectively.

The shape functions constructed by the variable s along contour coordinates of a cross-section including rigid body translations and rotations as well as higher-order deformations are introduced as:

$$\mathbf{\Psi} = \begin{Bmatrix} \mathbf{\Psi}_n(s) \\ \mathbf{\Psi}_s(s) \\ \mathbf{\Psi}_z(s) \end{Bmatrix} \tag{3}$$

Using Kirchhoff-Love assumptions, the displacements for arbitrary positions on a given cross-section are generally determined as follows:

$$\mathbf{u}^* = \begin{Bmatrix} u_n^* \\ u_s^* \\ u_z^* \end{Bmatrix} = \begin{Bmatrix} \bar{u}_n \\ \bar{u}_s - n\dfrac{\partial \bar{u}_n}{\partial s} \\ \bar{u}_z - n\dfrac{\partial \bar{u}_n}{\partial z} \end{Bmatrix} \tag{4}$$

Regard to other thin-walled theories, as an acceptable solution, shear strains at the mid-plane are usually negligible due to its complexity in multi-dimensional and multi-variable problems. However, in order to obtain results more accurate and fully capture the behavior of the thin-walled FG sandwich beam, these effects are also taken into account in this analysis. The strain vector in case of plane stress can be approximated as:

$$\epsilon = \begin{Bmatrix} \epsilon_s \\ \epsilon_z \\ \gamma_{sz} \end{Bmatrix} = \begin{Bmatrix} \dfrac{\partial u_s^*}{\partial s} \\ \dfrac{\partial u_z^*}{\partial z} \\ \dfrac{\partial u_z^*}{\partial s} + \dfrac{\partial u_s^*}{\partial z} \end{Bmatrix} \simeq \begin{Bmatrix} \left(\dfrac{\partial \mathbf{\Psi}_s(s)}{\partial s} - n\dfrac{\partial^2 \mathbf{\Psi}_n(s)}{\partial s^2}\right) \cdot \mathbf{U} \\ \mathbf{\Psi}_z(s)\dfrac{\partial \mathbf{U}}{\partial z} - n\mathbf{\Psi}_n(s)\dfrac{\partial^2 \mathbf{U}}{\partial z^2} \\ \mathbf{\Psi}_s(s)\dfrac{\partial \mathbf{U}}{\partial z} + \dfrac{\partial \mathbf{\Psi}_z(s)}{\partial s} \cdot \mathbf{U} - 2n\dfrac{\partial \mathbf{\Psi}_n(s)}{\partial s}\dfrac{\partial \mathbf{U}}{\partial z} \end{Bmatrix} \tag{5}$$

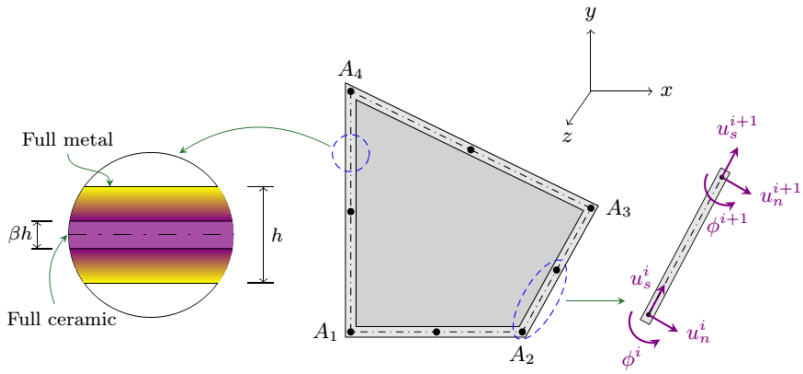

Figure 2. DOFs on each edge and material distribution through-the-thickness direction of a quadrilateral cross-section

In this paper, through the thickness direction, the sandwich material is adopted where ceramic material at middle plane is defined by βh ranging from $-0.5\beta h$ to $+0.5\beta h$ then approaches outwards to full metal both sides as shown in Fig. 2. The effective property as Young's modulus through-the-thickness direction can be determined via Young's modulus of metal E_{m} or ceramic E_{c} by relation:

$$E(n) = (E_c - E_m)V_c + E_m \tag{6}$$

where the ceramic's volume fraction is formulated as follows:

$$\begin{cases} V_{\mathrm{c}} = \left[\dfrac{-|n| + 0.5h}{0.5\,(1-\beta)\,h}\right]^k, & -0.5h \le n \le -0.5\beta h \text{ or } 0.5\beta h \le n \le 0.5h \\ V_{\mathrm{c}} = 1, & -0.5\beta h \le n \le 0.5\beta h \end{cases} \tag{7}$$

It should be emphasized that the power-law index k may be received a wide range value from 0 to infinity. This means when k is sufficiently large enough to approximate infinity, full metal will cover outside whereas fully ceramic thickness βh located at the middle. On the other hand, when k drops to zero the entire cross-section is now totally ceramic.

Concerning to the deformations, the energy with respect to strains and stresses within the given domain V is defined as follows:

$$\mathbf{U} = \frac{1}{2}\int_V \boldsymbol{\sigma}^T \epsilon dV = \frac{1}{2}\int_V \epsilon^T \mathbf{C}(n)\epsilon dV \tag{8}$$

where $\mathbf{C}(n)$ denotes stress-strain material matrix.

2.2. Beam frame modal

As reported in many studies, warping and distortion deformations contribute a major domination in behaviors of structures in which thin-walled beams with closed cross-section can be as a case. Several attempts have been made in order to tackle better for these difficult behaviors. For thin-walled closed profiles, it is seen from literature that beam frame model can achieve to more accurate results in practice since the lowest eigenmodes occur more frequently than others. For a given edge on each cross-section, a separated multi-beam Euler element is employed with a 3-degree-of-freedom node as described in Fig. 2.

The displacements are then calculated as follows:

$$\mathbf{U} = \mathbf{H}\mathbf{u} \tag{9}$$

where $\mathbf{u}$ and $\mathbf{H}$ refer to the so-called nodal displacement and displacement interpolation matrix, respectively, whereas linear Lagrange and Hermite cubic interpolation functions are included.

The nodal displacement vector for a element with nodes i^{th} and $(i+1)^{\text{th}}$ as depicted in Fig. 2 is defined as:

$$\mathbf{u} = \left\{ \begin{array}{cccccc} u_s^i & u_n^i & \phi^i & u_s^{i+1} & u_n^{i+1} & \phi^{i+1} \end{array} \right\}^T \tag{10}$$

The stiffness of an element for the beam frame modal can be derived as:

$$\mathbf{K}_e^{BF} = \int_V \mathbf{B}^{\mathrm{T}}\mathbf{C}\mathbf{B}dV = \int_0^{l_e}\int_0^{b_{BF}}\int_{-h/2}^{h/2} \mathbf{B}^T\mathbf{C}\mathbf{B}\mathrm{d}n\mathrm{d}z\mathrm{d}s \tag{11}$$

The explicit form of stiffness matrix in element level can be expressed as:

$$\mathbf{K}_e^{BF} = \begin{bmatrix} K_{11}^{BF} & K_{12}^{BF} & K_{13}^{BF} & K_{14}^{BF} & K_{15}^{BF} & K_{16}^{BF} \\ \vdots & K_{22}^{BF} & K_{23}^{BF} & K_{24}^{BF} & K_{25}^{BF} & K_{26}^{BF} \\ \vdots & & K_{33}^{BF} & K_{34}^{BF} & K_{35}^{BF} & K_{36}^{BF} \\ \vdots & & & K_{44}^{BF} & K_{45}^{BF} & K_{46}^{BF} \\ \vdots & & & & K_{55}^{BF} & K_{56}^{BF} \\ \text{sym.} & \dots & \dots & \dots & \dots & K_{66}^{BF} \end{bmatrix} \tag{12}$$

The global stiffness matrix $\mathbf{K}^{BF}$ are then obtained by collecting element stiffness matrices $\mathbf{K}_e^{BF}$ as (see more details in Appendix A):

$$\mathbf{K}^{BF} = \sum_{e=1}^{N} \mathbf{T}_e^T \mathbf{K}_e^{BF} \mathbf{T}_e \tag{13}$$

These above-mentioned equations are then systematically assembled to the typical eigenvalue problem as:

$$\begin{bmatrix} \mathbf{K}^{BF} & \mathbf{K}^{L} \\ \text{sym.} & \mathbf{0} \end{bmatrix} \left\{ \begin{array}{c} \boldsymbol{\Psi}^{\chi} \\ \boldsymbol{\varphi} \end{array} \right\} = \lambda \left\{ \begin{array}{c} \boldsymbol{\Psi}^{\chi} \\ \mathbf{0} \end{array} \right\} \tag{14}$$

where $\mathbf{K}^L$ is the constraint matrix, $\boldsymbol{\Psi}^{\chi}$ refers as nodal displacement vector, $\boldsymbol{\varphi}$ and λ are denoted as Lagrange multiplier and eigenvalue, respectively. In general, the orthogonality of distortions has been handled with regard to the in-plane displacements (x and y-coordinates) and rotation (about z axis) over entire area A as:

$$\begin{aligned} \int\int_A \psi_s^{\chi}\psi_s^{x}\mathrm{d}n\mathrm{d}s = 0 \\ \int\int_A \psi_s^{\chi}\psi_s^{y}\mathrm{d}n\mathrm{d}s = 0 \\ \int\int_A \psi_s^{\chi}\psi_s^{\theta}\mathrm{d}n\mathrm{d}s = 0 \end{aligned} \tag{15}$$

where distortion shape functions in contour direction are defined as ψ_s^{χ}; and ψ_s^{x}, ψ_s^{y}, ψ_s^{θ} are in-plane rigid body translations and rotation, respectively.

It should be mentioned here that distortion configurations are quite easily developed as a result of smaller energy distributions for the very first eigenmodes from Eq. (14) or the first two lowest mode for torsional distortion.

From the constant shear flow conditions, warping is then determined as

$$\psi_z^W(s) = \int_s \left(\frac{d\psi_s^\chi}{ds} ds \right) ds \tag{16}$$

The out-of-plane warping is completely checked for orthogonality with rigid body modes.

2.3. Finite element formulations

Through the axial direction of the beam, a two-noded element defined by i and j corresponding to two quadrilateral cross-sections I and J is considered. Noted that the planes containing these sections have been set to be always normal to the beam centerline. As a result, the center for each cross-section can be traced from one end to the another end. Therefore, taking this advantage, the beam can be extensively applied on different curvatures by adopting sufficient number of straight elements.

In order to describe the element, two sets of local coordinate systems which are mutually interrelated are employed as: (n_i, s_i, m_i) consists of m_i that is illustrated to be normal to the considered cross-section whereas s_i associated with contour direction and n_i is defined to be orthogonal to both s_i and m_i; (n_i, s_i, m_i) is indicated by setting n_i normal to mid-surface created by edge i^{th} (cross-sections I and J) whereas m_i specifies to mutually perpendicular to (n_i, s_i).

By using Eqs. (5) and (9), the strain vector can now be rewritten as:

$$\epsilon = \left\{ \begin{array}{c} \left(\dfrac{\partial \boldsymbol{\Psi}_s(s)}{\partial s} - n \dfrac{\partial^2 \boldsymbol{\Psi}_n(s)}{\partial s^2} \right) \cdot \mathbf{H} \\ \boldsymbol{\Psi}_z(s) \dfrac{\partial \mathbf{H}}{\partial z} - n \boldsymbol{\Psi}_n(s) \dfrac{\partial^2 \mathbf{H}}{\partial z^2} \\ \boldsymbol{\Psi}_s(s) \dfrac{\partial \mathbf{H}}{\partial z} + \dfrac{\partial \boldsymbol{\Psi}_z(s)}{\partial s} \cdot \mathbf{H} - 2n \dfrac{\partial \boldsymbol{\Psi}_n(s)}{\partial s} \dfrac{\partial \mathbf{H}}{\partial z} \end{array} \right\} \cdot \mathbf{u} = \mathbf{B}\mathbf{u} \tag{17}$$

where $\mathbf{B}$ refers as the strain-displacement matrix.

Using Eq. (8), variation of total potential energy is then expressed in general form as:

$$\begin{aligned} \delta\Pi &= \int_V \delta\mathbf{u}^T \mathbf{B}^T \mathbf{C}\mathbf{B}\mathbf{u} dV - \int_V \mathbf{f}\delta\mathbf{u} dV - \int_S \hat{\mathbf{t}}\delta\mathbf{u} dS \\ &= \delta\mathbf{u}^T \left(\int_V \mathbf{B}^T \mathbf{C}\mathbf{B} dV \right) \mathbf{u} - \mathbf{F}\delta\mathbf{u} \end{aligned} \tag{18}$$

where $\mathbf{f}$ and $\hat{\mathbf{t}}$ are the so-called body force vector and surface traction defined on an area S, respectively.

Finally, to derive the governing equation, the principle of minimum total potential energy can be stated as:

$$\delta\Pi = 0 \tag{19}$$

In order to describe stresses and strains, all components have to be performed in local coordinates. This transformation can generally be conducted through natural coordinates (ξ, η, ζ) and direction cosine vectors $\hat{\mathbf{n}}'_{ij}$ of $\left(n'_i, s_i, m'_i\right)$ by relation:

$$\nabla\mathbf{u}' = (\hat{\mathbf{n}}'_{ij})^T \cdot \nabla\mathbf{u} \cdot \hat{\mathbf{n}}'_{ij} \tag{20}$$

where

$$\nabla \mathbf{u} = \mathbf{J}^{-1} \cdot \nabla \mathbf{u}_{\xi\eta\zeta} \tag{21}$$

with **J** referring to the Jacobian matrix.

3. Numerical example

3.1. Numerical verification

To verify the accuracy of this study, displacements obtained from the analysis are compared to simulation results from ABAQUS. As a special case, the materials are set to be isotropic by using the gradation index $k = 0$. Properties of the beam are given as: Young's modulus $E = 200$ GPa, Poisson's ratio $\nu = 0.3$. A cantilever beam subjected to a couple $F_y = 1000$ N applied on the upper edge of a given cross-section which linearly varies from the fixed end ($z = 0$) to the tip ($z = L$) has been considered. The geometries of cross-sections are described as shown in Fig. 3 (unit: mm) with the thickness $h = 2$ mm and the length m.

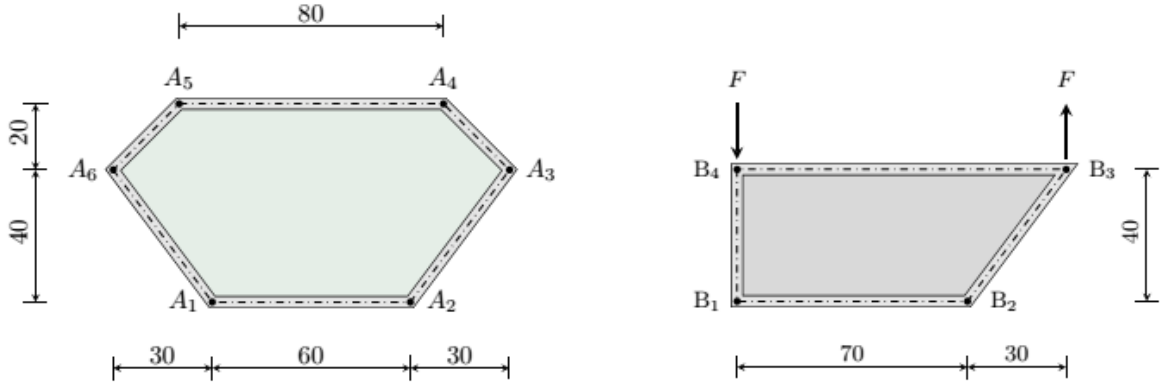

(a) Section at **z** = **0** (b) Section at **z** = **L**

Figure 3. Geometries and loading locations for numerical verification

Table 1. Non-dimensional displacements of the beam for comparison ($\times 10^{-2}$)

Method	z/L	0.0	0.2	0.4	0.6	0.8	1.0
This study	$\bar{u}_x$	0.0	0.0426	0.0796	0.1297	0.1709	−0.2570
	$\bar{u}_y$	0.0	−0.0268	−0.0824	−0.1340	−0.2259	−1.0197
	$\bar{u}_z$	0.0	−0.0012	−0.0013	0.0012	−0.0148	−0.0896
ABAQUS	$\bar{u}_x$	0.0	0.0427	0.0797	0.1290	0.1750	−0.2855
	$\bar{u}_y$	0.0	−0.0274	−0.0826	−0.1360	−0.2214	−1.0675
	$\bar{u}_z$	0.0	−0.0010	−0.0013	0.0013	−0.0144	−0.1003

The non-dimensional displacements $\bar{u}_{xyz} = \dfrac{Ehb^3_{|z=0}}{FL^3} u_{xyz}$ of a left-bottom point in x, y and z-axes along longitudinal direction of the beam are tabulated as shown in Table 1. From displayed results,

it can be observed that the numerically predicted displacements are in a good agreement with those obtained from ABAQUS. It should be mentioned that the solution can be achieved with only one interior node for each edge. However, a very small difference at the end may be seen in z-direction. From the above observations, it therefore can be concluded that the present model is able to reach a highly accurate results but spending less computational cost.

3.2. Flexural-torsional analysis

As a first example, the cantilever sandwich beam with cross-sections given in Fig. 4 is analyzed. Al_2O_3-Al material has been adopted in which alumina Al_2O_3 stands for ceramic (E_c = 380 GPa, ρ_c = 3960 kg/m^3) and aluminum Al refers as metal (E_m = 70 GPa, ρ_c = 2702 kg/m^3). Poisson's ratio ν and skin-core-skin factor β are 0.3 and 0.2, respectively.

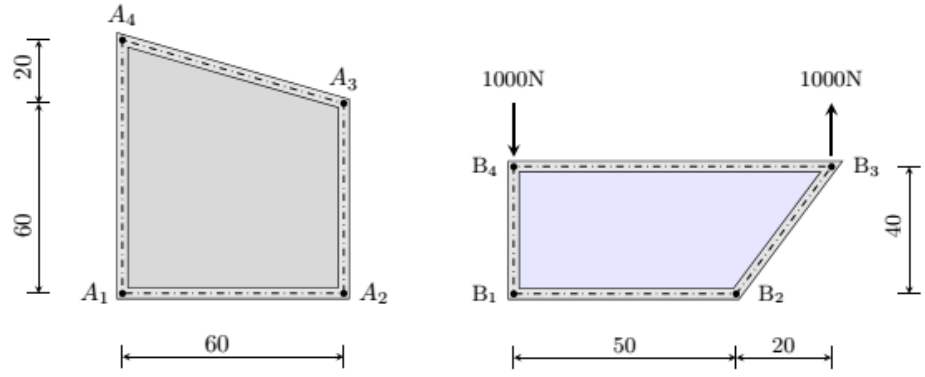

(a) Section at $\mathbf{z} = \mathbf{0}$ (b) Section at $\mathbf{z} = \mathbf{L}$

Figure 4. A varying quadrilateral cross-section and loading for flexural-torsional analysis

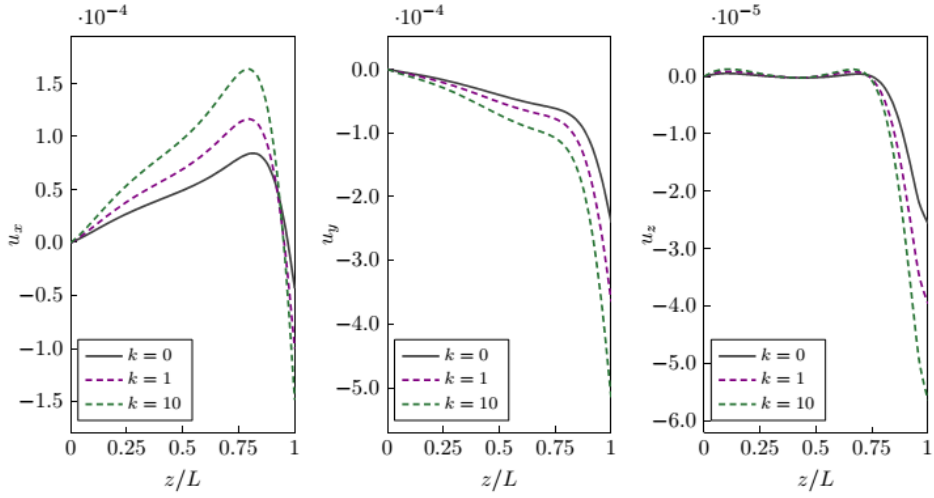

Figure 5. Displacements of points $A_1 - B_1$ in x, y, z-directions with various material distributions

In order to highlight the effect of material variations on deflections of the beam, the non-dimensional axial variable (z/L) versus displacements of points $A_1 - B_1$ is plotted as shown in Fig. 5.

From the figures, a large gap between three cases ($k = 0, 1, 10$) can be seen. The increase of k leads to a larger deflection. However, this is no longer true in x-axis. For z-direction, moreover, the beam is almost invariant from the fixed end to about 75% of L and then drops significantly till the tip. Conversely, in x-direction, the displacements of the beam tend towards different variations. The $2/3$ left beam's length moves upwards, whereas the others dramatically fall down. This fact can be explained due to the effects of material distributions, couplings and important role from distortions as well as warping as illustrated in Fig. 6. In addition, the couple force lying on a $x - y$ coordinate has a major dominance to its own plane rather than out-of-plane.

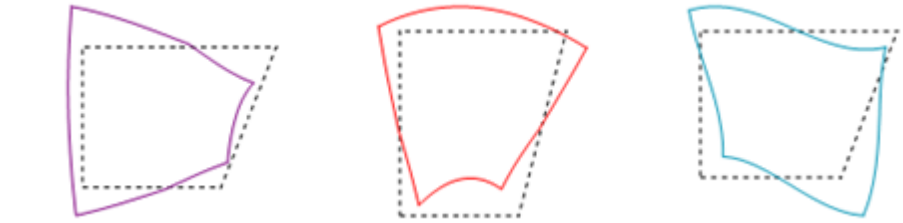

(a) In-plane distortion

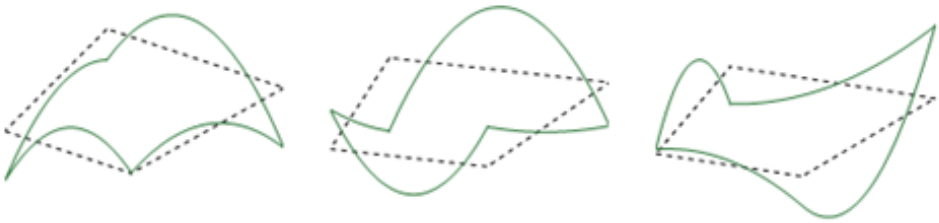

(b) Out-of-plane warping

Figure 6. Warping and distortion distributions in-plane and out-of-plane on the cross section

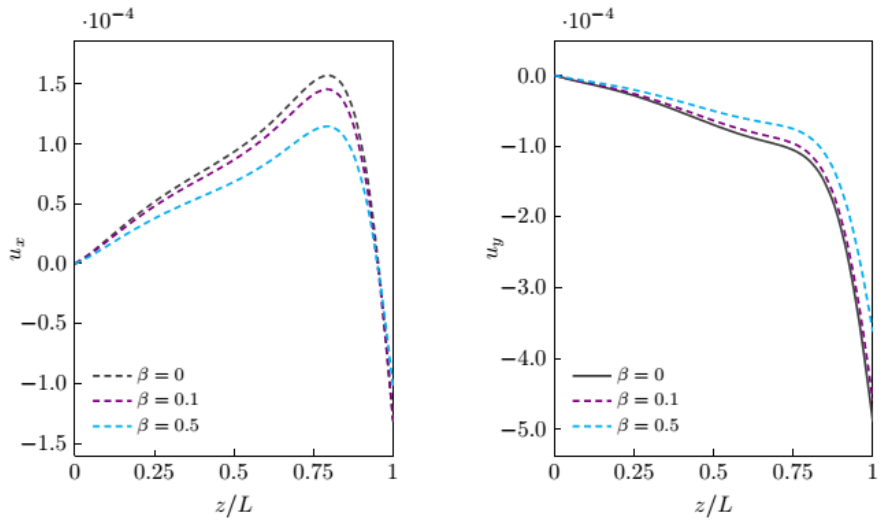

Figure 7. Effect of skin-core-skin on displacements in x- and y-directions with $k = 2$

The skin-core-skin effect related to material changes with various ratios β is performed as described in Fig. 7. As seen from the figures, the variation of β leads to distinct fluctuations. While the deflection in x-direction decreases as β increases, it develops inversely in y-axis. This phenomena can be clarified by the contribution of the stiffer through-the-thickness phase as ceramic that enhances the stiffness to be primary importance in y-axis but not in x-axis.

4. Conclusions

An analysis of general non-uniform quadrilateral cross-sections for thin-walled functionally graded sandwich beams has been presented. Generally, a prescribed shape function of ceramic is utilized to express through-the-thickness variation of materials. Based on beam frame modal and the framework of finite element method, a rigorous model of thin-walled structures applicable to both straight and curved beams is built. As a result, the approach has found to be profitable in terms of computational efficiency, adaptability and accuracy aspects. Through numerically obtained results and discussion, several remark outcomes can be drawn as follows:

- The established thin-walled model can extensively be applied on different curvatures by adopting straight multi-beam elements.

- Displacements of thin-walled FG beams are predominantly dependent on material distributions concerning to gradation index.

- Skin-core-skin ratio plays a major importance in contribution of flexural-torsional stiffness, and therefore significantly affects to behaviors of the beam.

Acknowledgements

This research is funded by Vietnam National Foundation for Science and Technology Development (NAFOSTED) under grant number 107.02-2019.33.

References

[1] Son, T., Huu-Tai, T. (2019). Free-vibration analysis of multi-directional functionally graded plates based on 3D isogeometric analysis. *Journal of Science and Technology in Civil Engineering (STCE)-NUCE*, 13 (2):1–11.

[2] Birman, V., Byrd, L. W. (2007). Modeling and analysis of functionally graded materials and structures. *Applied Mechanics Reviews*, 60:195–216.

[3] Vlasov, V. Z. (1961). *Thin-walled elastic beams*. Jerusalem, Israel, Program for Scientific Translation.

[4] Wekezer, J. W. (1989). Vibrational analysis of thin-walled bars with open cross sections. *Journal of Structural Engineering*, 115(12):2965–2978.

[5] Trahair, N. S., Bild, S. (1990). Elastic biaxial bending and torsion of thin-walled members. *Thin-Walled Structures*, 9(1-4):269–307.

[6] Bourihane, O., Braikat, B., Jamal, M., Mohri, F., Damil, N. (2016). Dynamic analysis of a thin-walled beam with open cross section subjected to dynamic loads using a high-order implicit algorithm. *Engineering Structures*, 120:133–146.

[7] Pandey, M. D., Kabir, M. Z., Sherbourne, A. N. (1995). Flexural-torsional stability of thin-walled composite I-section beams. *Composites Engineering*, 5(3):321–342.

[8] Volovoi, V. V., Hodges, D. H. (2000). Theory of anisotropic thin-walled beams. *Journal of Applied Mechanics*, 67(3):453–459.

[9] De Borbon, F., Mirasso, A., Ambrosini, D. (2011). A beam element for coupled torsional-flexural vibration of doubly unsymmetrical thin walled beams axially loaded. *Computers & Structures*, 89(13-14): 1406–1416.

[10] Kollár, L. P. (2001). Flexural–torsional buckling of open section composite columns with shear deformation. *International Journal of Solids and Structures*, 38(42-43):7525–7541.
[11] Nagashima, T., Suemasu, H. (2010). X-FEM analyses of a thin-walled composite shell structure with a delamination. *Computers & structures*, 88(9-10):549–557.
[12] Kim, H., Jang, G.-W. (2017). Higher-order thin-walled beam analysis for axially varying generally shaped cross sections with straight cross-section edges. *Computers & Structures*, 189:83–100.
[13] Aboudi, J., Pindera, M.-J., Arnold, S. M. (1999). Higher-order theory for functionally graded materials. *Composites Part B: Engineering*, 30(8):777–832.
[14] Wali, M., Hajlaoui, A., Dammak, F. (2014). Discrete double directors shell element for the functionally graded material shell structures analysis. *Computer Methods in Applied Mechanics and Engineering*, 278: 388–403.
[15] Librescu, L., Oh, S. Y., Song, O. (2004). Spinning thin-walled beams made of functionally graded materials: modeling, vibration and instability. *European Journal of Mechanics-A/Solids*, 23(3):499–515.

Appendix A.

The explicit expressions of stiffness matrices are obtained as:

$$
\begin{aligned}
K_{11}^{BF} &= \frac{E_c\beta h}{l_e} + \frac{(E_c + kE_m)(1-\beta)h}{(k+1)l_e}; & K_{14}^{BF} &= -\frac{E_c\beta h}{l_e} - \frac{(E_c + kE_m)(1-\beta)h}{(k+1)l_e} \\
K_{22}^{BF} &= \frac{\gamma_0 h^3 (E_c - E_m)}{l_e^3} + \frac{h^3 E_m}{l_e^3}; & K_{23}^{BF} &= \frac{\gamma_0 h^3 (E_c - E_m)}{2l_e^2} + \frac{h^3 E_m}{2l_e^2} \\
K_{25}^{BF} &= -\frac{\gamma_0 h^3 (E_c - E_m)}{l_e^3} - \frac{h^3 E_m}{l_e^3}; & K_{26}^{BF} &= \frac{\gamma_0 h^3 (E_c - E_m)}{2l_e^2} + \frac{h^3 E_m}{2l_e^2} \\
K_{33}^{BF} &= \frac{\gamma_0 h^3 (E_c - E_m)}{3l_e} + \frac{h^3 E_m}{3l_e}; & K_{35}^{BF} &= -\frac{\gamma_0 h^3 (E_c - E_m)}{2l_e^2} - \frac{h^3 E_m}{2l_e^2} \\
K_{36}^{BF} &= \frac{\gamma_0 h^3 (E_c - E_m)}{6l_e} + \frac{h^3 E_m}{6l_e}; & K_{44}^{BF} &= \frac{E_c\beta h}{l_e} + \frac{(E_c + kE_m)(1-\beta)h}{(k+1)l_e} \\
K_{55}^{BF} &= \frac{\gamma_0 h^3 (E_c - E_m)}{l_e^3} + \frac{h^3 E_m}{l_e^3}; & K_{56}^{BF} &= -\frac{\gamma_0 h^3 (E_c - E_m)}{2l_e^2} - \frac{h^3 E_m}{2l_e^2} \\
K_{66}^{BF} &= \frac{\gamma_0 h^3 (E_c - E_m)}{3l_e} + \frac{h^3 E_m}{3l_e}
\end{aligned}
\tag{A.1}
$$

where the coefficient γ_0 given by:

$$
\gamma_0 = \beta^3 + \frac{3(1-\beta)}{k+1} - \frac{6(1-\beta)^2}{k+2} + \frac{3(1-\beta)^3}{k+3} \tag{A.2}
$$

Others are zeros.

The transformation matrix $\mathbf{T}_e$ can be expressed as:

$$
\mathbf{T}_e = \begin{bmatrix}
\cos\alpha_e & \sin\alpha_e & 0 & 0 & 0 & 0 \\
 & -\cos\alpha_e & 0 & 0 & 0 & 0 \\
 & & 1 & 0 & 0 & 0 \\
 & & & \cos\alpha_e & \sin\alpha_e & 0 \\
 & & & & -\cos\alpha_e & 0 \\
\text{sym.} & & & & & 1
\end{bmatrix} \tag{A.3}
$$